Available online at www.sciencedirect.com
SCIENCE DIRECT
Journal of Catalysis 239 (2006) 486–500
JOURNAL OF CATALYSIS
www.elsevier.com/locate/jcat

Synthesis and characterization of novel silica-supported Pd/Yb bimetallic catalysts: Application in gas-phase hydrodechlorination and hydrogenation

Satyakrishna Jujjuri [a], Errun Ding [b], Elizabeth L. Hommel [b], Sheldon G. Shore [b], Mark A. Keane [c,*]

[a] *Department of Chemical and Materials Engineering, University of Kentucky, USA*
[b] *Department of Chemistry, The Ohio State University, USA*
[c] *Chemical Engineering, School of Engineering and Physical Sciences, Heriot-Watt University, Edinburgh EH14 4AS, Scotland, UK*

Received 17 November 2005; revised 15 February 2006; accepted 25 February 2006

Abstract

The gas-phase hydrodechlorination (HDC) of chlorobenzene (CB), 1,2-dichlorobenzene (1,2-DCB), and 1,3-dichlorobenzene (1,3-DCB) was investigated over a 5% w/w Pd/SiO_2 and a series of SiO_2-supported Yb–Pd (5% w/w Pd and Yb/Pd = 2/3 mol/mol) catalysts. The Pd/SiO_2 catalyst was prepared by $Pd(C_2H_3O_2)_2$ impregnation, supported Yb synthesized by contacting SiO_2 with Yb powder in liquid NH_3 and the bimetallic catalysts prepared by two stepwise routes: $Pd(C_2H_3O_2)_2$ impregnation of Yb/SiO_2 (Pd–Yb/SiO_2-step) or Pd impregnation preceding Yb introduction (Yb–Pd/SiO_2-step) and a single-step simultaneous introduction of Pd and Yb from a $\{(DMF)_{10}Yb_2[Pd(CN)_4]_3\}_\infty$ precursor ($Yb/Pd/SiO_2$-sim). Under identical reaction conditions, the following specific initial CB HDC rate sequence was established: Pd–Yb/SiO_2-step (0.21 $mol_{Cl}\,h^{-1}\,m^{-2}$) ≈ Pd/SiO_2 (0.24 $mol_{Cl}\,h^{-1}\,m^{-2}$) < $Yb/Pd/SiO_2$-sim (0.41 $mol_{Cl}\,h^{-1}\,m^{-2}$) ≈ Yb–Pd/SiO_2-step (0.46 $mol_{Cl}\,h^{-1}\,m^{-2}$); reaction over Yb/SiO_2 resulted in a negligible conversion. Yb acts as a CB HDC promoter through a surface synergism with Pd; the extent of this promotion depends on the nature of the catalyst precursor and the sequence of metal(s) introduction to the support. The promotional effect of Yb extends to DCB HDC, where Yb–Pd/SiO_2-step outperforms $Yb/Pd/SiO_2$-sim (with a specific HDC rate 25 times greater than that delivered by Pd/SiO_2) and to catalytic hydrogenation (benzene → cyclohexane). The prereaction and postreaction catalyst samples were characterized in terms of BET area, TPR, TEM-EDX, H_2 chemisorption/TPD, XRD, and XPS measurements. The role of Yb as a promoter is discussed in terms of electron donation and impact on Pd dispersion but is attributed to the action of YbH_2, which serves as an additional source of surface reactive hydrogen; Yb activation of the C–Cl bond(s) for hydrogenolytic attack is also considered. HDC activity decreased with time-on-stream, an effect that we link to deleterious HCl/catalyst interactions that modify surface composition, leading to a disruption in H_2 uptake/release; XPS and TEM-EDX were used to characterize the residual surface Cl post-HDC.

Keywords: Hydrodechlorination; Pd/SiO_2; Silica-supported Yb/Pd; Chlorobenzene; Dichlorobenzene; YbH_2; Catalyst deactivation

1. Introduction

The importance of hydrodechlorination (HDC) (i.e., H_2 scission of C–Cl bonds) has shifted somewhat from an organic synthetic step [1,2] to an environmental remediation strategy [3,4]. Chloro-emissions into the environment are now stringently regulated, due to the associated adverse health effects and ecological damage [5]. Disposal of chlorinated waste by incineration is highly energy demanding, and incomplete combustion can lead to furan/dioxin release [6]. Catalytic HDC is emerging as an alternative low-energy, nondestructive methodology that facilitates recovery/reuse of valuable chemical feedstock [7]. Heterogeneous catalytic HDC has now been reported for liquid-phase [8–25] and gas-phase [26–59] operations, involving aliphatic reactants [8,11,16,27–29,31–36,39,43–45] and aromatic reactants [3,9,10,12–15,17–26,28,30,37–42,46–59]. There have been some attempts at kinetic modeling [17–19,26,28,46–52], but most reports have recorded HDC activities/selectivities over a particular, often narrow, range of operating conditions. In this study, we report the results of gas-phase chlorobenzene (CB) and dichlorobenzene(s) (DCB) HDC

* Corresponding author.
E-mail address: m.a.keane@hw.ac.uk (M.A. Keane).

0021-9517/$ – see front matter
doi:10.1016/j.jcat.2006.02.022

over silica-supported Pd and Yb/Pd that will add to and significantly extend the existing corpus of work on gas-phase [28,30,50,51,54–59] and liquid-phase [12,13,15] chloroarene HDC promoted by supported Pd catalysts. The above represents a compilation of the literature that is of direct relevance to this study; we relate our results, where feasible, to the published data.

It is accepted that catalytic HDC, in common with most hydrogenolysis reactions, is strongly influenced by the electronic structure of the active metal sites [60]. Some consensus is now emerging that HDC efficiency is sensitive to metal loading and the nature of the support, with higher specific HDC activities achieved at lower Pd [54,61] and Ni [62–64] dispersions. Moreover, Gopinath et al. [56] observed both an increase in activity and a greater resistance to deactivation during CB HDC over larger Pd particles (38 vs. 25 nm) on Nb_2O_5. Indeed, catalyst deactivation has been a common feature of HDC systems, ascribed to coke deposition [65], formation of surface metal halides [30,66,67], or metal sintering [68]. In an earlier paper [69], we reported preliminary results that demonstrated an appreciably higher chloroarene HDC over bimetallic Yb–Pd/SiO_2 compared with Pd/SiO_2. Coq and Figueras, in a comprehensive review [70], noted that bimetallic Pd catalysts exhibit elevated HDC activities relative to the corresponding monometallic when the second metal serves as an electron donor. We tentatively attributed the promotional effect of the electropositive Yb to electron donation and/or hydrogen transfer via surface YbH_2 [69] and showed that this promotional effect extended to aromatic hydrogenation [71]. There are reports of homogeneous liquid-phase lanthanide catalytic applications in the dehalogenation of olefinic [72] and aromatic [73,74] halides with NaH as a reductant. However, an extensive search through the literature did not reveal any study dealing with HDC over lanthanide-promoted supported Pd catalysts. Nevertheless, we can flag related studies concerning the hydrogenation of propyne (Pd–Yb(Eu)/SiO_2) [75], ethylbenzene (Pd–La/SiO_2) [76], and acryclic acid (Ln–Pd/polyacrylate (PAA), Ln = Nd, Sm, Eu, Gd, Tb, Er, Yb, Lu) (homogeneous catalysis) [77], where an increased activity was recorded for the bimetallic catalysts. Imamura et al. [75] linked an improved propyne hydrogenation over Yb-promoted Pd/SiO_2 (compared with Pd/SiO_2) to an enhanced hydrogen uptake. In a subsequent study [78] of ethylene hydrogenation over Eu and Yb supported on MnO, MgO, and TiO_2, the same authors demonstrated critical catalytic responses to lanthanide loading and catalyst pretreatment. In our earlier work [69], Yb/Pd/SiO_2 was synthesized from a $\{(DMF)_{10}Yb_2[Pd(CN)_4]_3\}_\infty$ precursor, that is, simultaneous addition of Pd and Yb to the SiO_2 carrier. In the present study, we extend the earlier study to consider the action of Yb–Pd/SiO_2 prepared by stepwise Yb/Pd addition, providing new catalyst characterization (BET, TPR, H_2-chemisorption/TPD, TEM-EDX, XRD and XPS) results to supplement additional catalytic data. We also consider haloarene reactivity by comparing the HDC of CB with DCB. The available literature on DCB HDC [15,23,24,28,30] is somewhat fragmented, with some evidence [23,24] of differences in DCB isomer reactivity, an effect that we address in this report. Moreover, we examine catalyst structural changes during HDC by subjecting the postcatalysis samples to the same characterization analyses.

2. Experimental

2.1. Catalyst preparation and activation

The Pd/Yb complex $\{(DMF)_{10}Yb_2[Pd(CN)_4]_3\}_\infty$, which served as the bimetallic catalyst precursor, was prepared using a procedure previously described by Shore et al. [79]. A solution of the bimetallic complex in DMF was contacted with SiO_2 (fumed; Sigma-Aldrich) to deliver a 5% w/w Pd loading. The DMF was extracted from the metal-impregnated SiO_2 under vacuum over 12 h at room temperature. The resulting white solid was removed in air and placed (in a quartz boat) in a furnace and flushed with H_2 for ca. 10 min and reduced under a steady H_2 flow at ca. 10 K min^{-1} to a final temperature of 523 K, which was maintained for 30 min. The sample was then flushed in He and passivated in a 1% v/v O_2 in He flow at room temperature. A monometallic 5% w/w Pd/SiO_2 was prepared by contacting the same SiO_2 substrate with $Pd(C_2H_3O_2)_2$ in DMF with subsequent activation/passivation as above; details are provided elsewhere [71]. Yb/SiO_2 was prepared by charging known amounts of SiO_2 and Yb powder into a reaction flask (located in a dry box) with vacuum transfer of liquid NH_3 into the flask at 195 K. The mixture was kept under constant agitation for ca. 3 h, at which point the NH_3 was pumped away. Silica supported Yb/Pd bimetallics (2/3 mol ratio, 5% w/w Pd) were prepared in a stepwise fashion, with Pd introduction preceding Yb (denoted as Yb–Pd/SiO_2-step) or Yb added first, followed by impregnation with $Pd(C_2H_3O_2)_2$ (i.e., the Pd–Yb/SiO_2-step); both bimetallics were reduced and passivated as above. The supported bimetallic generated from $\{(DMF)_{10}Yb_2[Pd(CN)_4]_3\}_\infty$ is denoted herein as Yb/Pd/SiO_2-sim. A physical mixture of Pd/SiO_2 and Yb/SiO_2 with the same Pd/Yb mol ratio was also considered and is denoted as Pd/SiO_2 + Yb/SiO_2. The metal loadings were determined (to within ±2%) by inductively coupled plasma-optical emission spectrometry (ICP-OES; Vista-PRO, Varian) from the diluted extract of aqua regia. Each sample was sieved (ATM fine test sieves) into a batch of 75 μm average particle diameter and subjected to a second reduction step (before catalysis) in a fixed-bed tubular glass reactor (1.25 cm i.d.) by heating (at a rate of 10 K min^{-1}) in a 60 cm^3 min^{-1} stream of dry H_2 (99.999%), monitored using a Humonics (Model 520) flow meter to a final temperature of 573 K, which was maintained for 12 h.

2.2. Catalyst characterization

Both activated unused (denoted as pre-HDC) and used (after 18 h on stream, denoted as post-HDC) passivated catalyst samples were characterized. BJH pore volume analyses were performed using the commercial Micromeritics TriStar 3000 unit, with N_2 at 77 K serving as a sorbate. BET surface area, temperature-programmed reduction (TPR), H_2 chemisorption,

and temperature-programmed desorption (TPD) were determined using the commercial CHEM-BET 3000 (Quantachrome) unit. Total surface area was recorded in a 30% v/v N_2/He flow, with pure N_2 (99.9%) as the internal standard. After outgassing for 30 min, at least two cycles of N_2 adsorption–desorption in the flow mode were conducted using the standard single-point BET method. Immediately after BET measurement, the samples (ca. 50 mg fresh and spent) were heated in a U-shaped quartz cell (21 cm × 3.76 mm i.d.) in 20 $cm^3\,min^{-1}$ (Brooks mass flow controller) 5% v/v H_2/N_2 to 573 K at 10 $K\,min^{-1}$, and the effluent gas was passed through a liquid N_2 trap; changes to the carrier gas composition were monitored with a thermal conductivity detector (TCD) with data acquisition/manipulation using the TPR Win software. The samples were swept with 20 $cm^3\,min^{-1}$ dry N_2 for 1 h at 573 K, cooled to room temperature, and subjected to H_2 chemisorption using a pulse (50 μL) titration procedure. Any possible contribution due to β-palladium hydride formation was avoided as the H_2 partial pressure was <2 Torr, well below the pressure (>11 Torr) required to generate the hydride [30]. The sample was thoroughly flushed with N_2 (20 $cm^3\,min^{-1}$) for 30 min to remove any weakly bound H_2. TPD was conducted in the N_2 flow at 50 $K\,min^{-1}$ up to 1273 K, with a final isothermal hold of 15 min. Based on TCD calibrations and analysis of the effluent gas using a MICROMASS PC Residual Gas Analyser, the TPD profiles recorded in this paper can be attributed solely to H_2 release. The BET surface areas and H_2 uptake values were reproducible to within ±5%; the values quoted in this paper are the mean.

Transmission electron microscopy (TEM) analysis was conducted using a JEOL-2000 TEM/STEM microscope equipped with a UTW energy dispersive X-ray (EDX) detector (Oxford Instruments) and operated at an accelerating voltage of 200 kV. The specimens were prepared by ultrasonic dispersion in 2-butanol, evaporating a drop of the resultant suspension onto a lacey carbon support grid. The mean Pd particle sizes quoted in this study are based on a measurement of more than 600 individual particles. Powder X-ray diffraction (XRD) data were collected on a Bruker D8 Advance X-ray powder diffractometer (Cu-K_α radiation) from samples (subjected to a reductive atmosphere at 523 or 873 K) loaded in 0.5 mm Lindeman glass capillaries in a glove box and sealed. X-Ray photoelectron spectroscopic (XPS) analyses were conducted using a Kratos Axis Ultra spectrometer with monochromatized Mg-K_α radiation (1253.6 eV). A sample of activated/passivated catalyst was adhered to conducting carbon tape, mounted in the sample holder, and subjected to UHV conditions (ca. 10^{-9} Torr) overnight before analysis. Full-range surveys (0–1000 eV) and high-resolution spectra of Pd $3d_{3/2}/3d_{5/2}$, Yb $4d_{5/2}$, Si 2p, O 1s, Cl $2p_{3/2}$, and C 1s were collected. Physical mixtures of $PdCl_2 + SiO_2$ and $YbCl_3 + SiO_2$ served as reference samples. The C 1s peak, centered at 284.5 eV, was used as reference to calibrate the binding energy values. The signals for Pd, Yb, and Cl were much weaker than those for Si and O, due to the low concentrations in the SiO_2 matrix. Thus, extended scans were used to improve signal-to-noise ratio; the tabulated binding energy values, obtained from a Gaussian fit, were reproducible to ±0.05 eV.

2.3. Catalytic system

The reactions were conducted in situ (after catalyst activation) with a co-current flow of the aromatic feed in H_2. A layer of glass beads above the catalyst bed ensured that the reactants were vaporized and reached reaction temperature before contacting the catalyst [39]. A microprocessor-controlled infusion pump (kd Scientific model 100) was used to deliver the feed through a glass/Teflon airtight syringe and Teflon line at a fixed calibrated flow rate. All of the HDC reactions were carried out at 423 K, where isothermal operation was ensured by diluting the catalyst bed with ground glass (75 μm). CB (Aldrich, 99.9% v/v), 1,2-DCB (Aldrich, 99% v/v), 1,3-DCB (Aldrich, 99% v/v), and methanol solvent (Merck, 99.8% v/v) were used without further purification. The HDC reaction was monitored at an inlet hourly Cl/Pd molar ratio of 5×10^3 and a contact time of 0.02 min. In a series of blank tests, passage of each reactant in a stream of H_2 through the empty reactor (i.e., in the absence of catalyst) did not result in any detectable conversion. The reactor effluent was frozen in a liquid nitrogen trap for subsequent analysis performed using a Perkin-Elmer Auto System XL chromatograph equipped with a split/splitless injector and a flame ionization detector, with a DB-1 50 m × 0.20 mm i.d., 0.33 μm capillary column (J&W Scientific). The overall level of HDC was converted to mol% conversion using detailed calibration plots for each feedstock. Quantitative analysis was based on relative peak area with acetone as a solvent; analytical repeatability was better than ±1%, and the detection limit typically corresponded to a feedstock conversion of <0.1 mol%. HDC performance is quantified in terms of fractional dechlorination (x_{Cl}),

$$x_{Cl} = \frac{[Cl_{org}]_{in} - [Cl_{org}]_{out}}{[Cl_{org}]_{in}}, \tag{1}$$

where $[Cl_{org}]$ represents concentration (mol dm^{-3}) of chlorine associated with the aromatic feed and subscripts "in" and "out" refer to the inlet and outlet reactor streams, respectively. It has been demonstrated previously [39,47,49] that HCl is the only inorganic product with no detectable Cl_2 production, that is, $[Cl_{org}]_{in} - [Cl_{org}]_{out} = [HCl]_{out}$. The percentage selectivity of chlorobenzene (S_{CB} %) from the DCB feed is given by

$$S_{CB}\ (\%) = \frac{[CB]_{out}}{[DCB]_{in} - [DCB]_{out}} \times 100. \tag{2}$$

Repeated reactions with different samples from the same batch of catalysts delivered raw data reproducibility better than ±5%. Hydrogenation activity was also monitored by examining the reduction of benzene (as feed) at 423 K; the inlet hourly benzene/Pd molar ratio was 35. The catalyst was activated as above, and benzene conversion was monitored for 3 h on stream. The catalyst was then contacted with 0.3 mol 1,2-DCB over 24 h, and the benzene feed was reintroduced with product analysis; cyclohexane was the only product detected. The

percentage yield of cyclohexane ($Y_{\text{cyclohexane}}$ %) is defined as

$$Y_{\text{cyclohexane}}\ (\%) = \frac{[\text{cyclohexane}]_{\text{out}}}{[\text{benzene}]_{\text{in}}} \times 100. \quad (3)$$

3. Results and discussion

3.1. Catalyst characterization pre-HDC

3.1.1. BET/TPR/XRD

The BET area of Pd/SiO_2 was close to that of the starting SiO_2 (200 $m^2\ g^{-1}$), whereas all of the Yb-containing (Yb/SiO_2, Pd–Yb/SiO_2-step, Yb–Pd/SiO_2-step, and $Yb/Pd/SiO_2$-sim) samples exhibited markedly smaller areas (Table 1). This may be attributed to partial pore filling by the Yb component, as is borne out by the lower pore volumes recorded in Table 1. Indeed, we showed in previous work [69] that Yb in the activated $Yb/Pd/SiO_2$-sim was present as a "thin film" with no evidence of surface Yb particle or cluster formation. Pore blocking appears to extend to the stepwise preparation as well. The TPR profiles of the passivated samples are shown in Fig. 1; each profile exhibits a characteristic negative peak (H_2 release) at 366 ± 6 K (Table 2). A similar release of H_2 from supported Pd has been reported by several authors [80–91] over the temperature range 323–373 K, ascribed to the decomposition of Pd hydride formed during H_2 contact at room temperature. The absence of any obvious H_2 consumption (during TPR) in advance of H_2 release presupposes the existence of the metallic phase before the initiation of the temperature ramp. Indeed, a room temperature reduction of PdO has been recorded in the literature [80–83]. But an ill-defined H_2 consumption in the TPR profile for Pd/SiO_2 at 573 K (Fig. 1b) is indicative of a (not insignificant) temperature-induced reduction step, which is in line with previous reports [92,93]. The XRD patterns given in Fig. 2 provide important bulk structural characteristics for the activated catalysts. The pattern associated with Pd/SiO_2 is consistent with an exclusive cubic symmetry in which the *d* spacings (2.24801, 1.94622, 1.37579, 1.17231, 1.12192, and 1.00515 Å) and relative intensities are in excellent agreement with those reported by Kern and Eysel [94]. A range of Pd hydride compositions has been quoted in the literature [95,96], with a limiting value of H/Pd in bulk Pd of 0.76 [97]. Higher H/Pd ratios have been attributed to a trapping in and/or spillover of hydrogen onto the support [96]. Our experimentally determined H/Pd ratios are recorded in Table 2; the value for Pd/SiO_2 (0.34) is close to those values quoted in the literature for Pd/SiO_2 [98] and Pd/C [87]. A similar H/Pd ratio was obtained for Pd–Yb/SiO_2-step and the $Pd/SiO_2 + Yb/SiO_2$ physical mixture (0.30), but a markedly lower ratio characterized Yb–Pd/SiO_2-step and $Yb/Pd/SiO_2$-sim. Given the lower H/Pd ratio associated with Yb–Pd/SiO_2-step relative to Pd–Yb/SiO_2-step, adding Yb to Pd/SiO_2 appears to inhibit hydride formation. It is worth noting that Batista et al. [83] did not observe a negative peak in their TPR profile for alumina-supported Pd/Cu, and they attributed the absence of hydride to alloy formation. Nag [87] observed a decreased H/Pd ratio as a result of

Table 1
Nitrogen BET surface areas and pore volumes, pre- and post-HDC

	Pre-HDC		Post-HDC
	BET area ($m^2\ g^{-1}$)	Pore volume ($cm^3\ g^{-1}$)	BET area ($m^2\ g^{-1}$)
Pd/SiO_2	191	1.4	184
Yb/SiO_2	160	1.0	–[a]
Pd–Yb/SiO_2-step	155	1.0	152
Yb–Pd/SiO_2-step	156	1.1	137
$Yb/Pd/SiO_2$-sim	163	0.9	153

[a] HDC inactive.

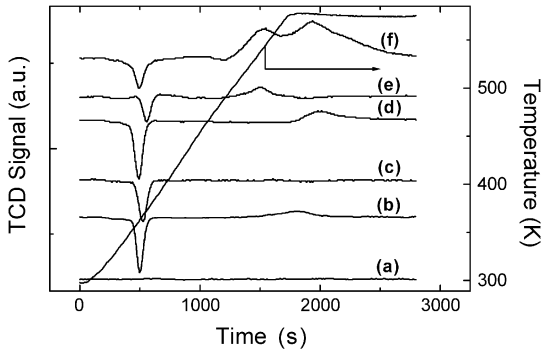

Fig. 1. TPR profiles of the passivated catalysts, pre-HDC: (a) Yb/SiO_2, (b) Pd/SiO_2, (c) $Pd/SiO_2 + Yb/SiO_2$, (d) Pd–Yb/SiO_2-step, (e) Yb–Pd/SiO_2-step, (f) $Yb/Pd/SiO_2$-sim.

Table 2
Temperature related peak maxima ($T_{\max}$) associated with the TPR profiles pre- and post-HDC and the H/Pd mol ratios corresponding to Pd hydride decomposition

	Pre-HDC		Post-HDC	
	TPR $T_{\max}$ (K)	H/Pd	TPR $T_{\max}$ (K)	H/Pd
Pd/SiO_2	**371**, 573	0.34	**374**	0.59
Pd–Yb/SiO_2-step	**367**, 573	0.33	**371**, 437	0.30
Yb–Pd/SiO_2-step	**372**, 532	0.13	**372**, 409, 441	0.16
$Yb/Pd/SiO_2$-sim	**361**, 544, 573	0.22	**373**, 438, 573	0.21

$T_{\max}$ for H_2 release given in bold.

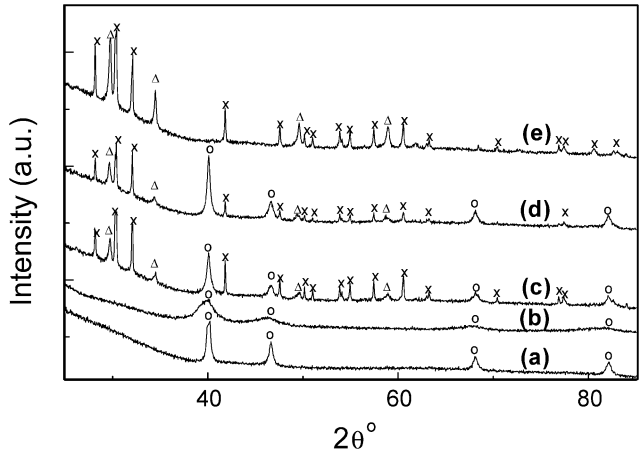

Fig. 2. XRD of the catalysts reduced at 573 K, pre-HDC: (a) Pd/SiO_2, (b) $Yb/Pd/SiO_2$-sim, (c) Pd–Yb/SiO_2-step, (d) Yb–Pd/SiO_2-step, (e) Yb/SiO_2. Note O indicates peak assignment for Pd (*fcc*), X for YbH_2 (orthorhombic), Δ for $Yb(NH_2)_x$ (*bcc*-tetragonal) and Yb_2O_3 (cubic).

increasing Pd dispersion on a carbon support and proposed that both the ratio and the decomposition temperature (T_{max}) were raised with increasing metal crystallite size due to a stronger binding force holding the hydride in the metal lattice, that is, a T_{max} increase from 330 to 350 K with an associated H/Pd increase from 0.1 to 0.26 for a Pd size increase from 25 to 105 Å. Pinna et al. [98] attributed the higher temperature shift in H_2 release to a greater stability of the hydride and/or a greater ordering of crystallites in larger particles, which serves to delay H migration to the surface through diffusion effects [98]. There is, however, no obvious correlation between the H/Pd and T_{max} values recorded in this study, where hydride suppression results from Yb modification of surface Pd through the simultaneous addition of both metals (Yb/Pd/SiO_2-sim) and the introduction of Yb to Pd/SiO_2 (Yb–Pd/SiO_2-step).

The TPR profile (to 573 K) for Yb/SiO_2 is featureless (see Fig. 1) without any evidence of H_2 uptake or release. In the preparation of Yb/SiO_2 and stepwise synthesis of the Yb/Pd bimetallic catalysts, Yb is introduced by dissolving in liquid NH_3 with the formation of $Yb(NH_2)_3/Yb(NH_2)_2$ [78]. XRD analysis of the activated samples has revealed the presence of YbH_2, $Yb(NH_2)_x$ and Yb_2O_3 [99], as shown in Fig. 2; *bcc*-tetragonal-$Yb(NH_2)_2$ and cubic-Yb_2O_3 have similar strong reflections and cannot be decoupled/identified unambiguously. The absence of an exclusive Yb phase is not unexpected, because the generation of metallic Yb under atmospheric pressure requires a (carbothermal) reduction treatment at temperatures in excess of 2000 K [100]. There was no evidence (on the basis of XRD analysis) of bulk alloy formation in the three bimetallic catalysts, and only reflections that are characteristic of metallic Pd were detected. The three bimetallic catalysts generated broad, higher-temperature ($T_{max} > 530$ K) H_2 consumption peaks that extend into the final isothermal hold (see Fig. 1). Although an exhaustive search through the literature failed to unearth any directly comparable published TPR analysis of supported Yb/Pd, we can draw on the results of some pertinent catalyst characterization studies. Fígoli et al. [76] reported an increase in reduction temperature (from 367 to 403 K) with increasing amounts of La_2O_3 addition to Pd/SiO_2 and linked this response to a blocking effect by the lanthanide that hinders the reduction of PdO; they claim that La_2O_3 is not reduced over the temperature range of 273–973 K. Yang et al. [84] also reported an inhibited reduction of PdO supported on γ-Al_2O_3 due to the addition of La_2O_3 with a shift in T_{max} by up to 40 K (from $T_{max} = 353$ K for PdO/γ-Al_2O_3). Weyrich et al. [85] observed two TPR peaks (at 570 and 740 K) attributed to the reduction of CeO_2 supported on Na-ZSM5. A contribution due to nonstoichiometric Yb_2O_{3+x} reduction (to Yb_2O_3, detected by XRD) may account, at least in part, for the H_2 consumption peaks that we have recorded. Indeed, in a subsequent TPR of Yb/SiO_2 to 1273 K (not shown), there was evidence of H_2 consumption at ca. 760 K, which can be attributed to oxide reduction. A lower Yb_2O_{3+x} reduction temperature for the supported bimetallics may be the result of a Pd-promoted TPR with the possible involvement of spillover H_2, as was proposed by Weyrich et al. [85], where Pd acts as a dissociation center to generate reactive hydrogen, which then spills over to the support. The XRD pattern for Yb/Pd/SiO_2-sim revealed only the presence of crystalline Pd species, an observation in accordance with our earlier TEM–EDX detection of Yb as a surface film [71,101]; any Yb oxide that may be present does not contribute to the XRD pattern, possibly due to a high degree of dispersion. The broad character of the Pd diffraction maxima in Yb/Pd/SiO_2-sim suggests short-range order. The lower TPR T_{max} (532 K) associated with Yb–Pd/SiO_2-step when compared with Pd–Yb/SiO_2-step (573 K) is significant, as too is the occurrence of two regions of H_2 consumption for Yb/Pd/SiO_2-sim. We cannot explicitly identify an exclusive source of this H_2 consumption, but suggest at this juncture that it may arise from Yb interactions that influence the secondary PdO reduction temperature and/or a possible contribution due to Yb_2O_{3+x} reduction.

Table 3
H_2 uptakes (after TPR to 573 K), pre- and post-HDC

	H_2 uptake ($\mu mol\, g_{cat}^{-1}$)	
	Pre-HDC	Post-HDC
Pd/SiO_2	6	2
Yb/SiO_2	1	–[a]
Pd–Yb/SiO_2-step	7	2
Yb–Pd/SiO_2-step	21	21
Yb/Pd/SiO_2-sim	35	39

[a] HDC inactive.

3.1.2. H_2 chemisorption/TPD

The H_2 chemisorption values are given in Table 3. We have avoided the assignment of Pd particle sizes or dispersion based on the chemisorption measurements, because this presumes an exclusive H:Pd stoichiometry, which is at best a convenient approximation, whereas possible contributions to uptake due to the presence of Yb further mitigate against a valid metal size assignment. Uptake on Yb/SiO_2 was considerably lower than that delivered by Pd/SiO_2; XRD analysis (see Fig. 2e) established the presence of YbH_2 formed during TPR, which accounts for limited uptake capacity in the subsequent room temperature H_2 pulse experiments. Chemisorption on Pd/SiO_2 was conducted under conditions in which Pd hydride formation was circumvented, as explained in the Experimental section. Uptake on the Pd/SiO_2 + Yb/SiO_2 physical mixture (5 $\mu mol\, g^{-1}$) and the Pd–Yb/SiO_2-step sample was equivalent to that obtained for Pd/SiO_2, indicating the absence of any significant chemical interaction, in keeping with the common H/Pd hydride ratios. In marked contrast, the Yb–Pd/SiO_2-step and Yb/Pd/SiO_2-sim samples exhibited a threefold and fivefold increase in H_2 uptake, respectively, relative to Pd/SiO_2 (and Pd–Yb/SiO_2-step). Increased H_2 uptake was also observed by Imamura et al. [75] during the hydrogenation of C_3H_4 with Yb-promoted Pd/SiO_2 catalyst, a system similar to our Yb–Pd/SiO_2-step; however, in their work, Pd/SiO_2 was first reduced before being impregnated with Yb. Moreover, their observed H_2 enrichment required the presence of C_3H_4; the same response was not observed after introduction of C_2H_2. Seaone et al. [89] reported a higher H_2 uptake on a coimpregnated La/Pd/SiO_2 (after calcination/reduction) and attributed this effect to the formation of smaller Pd particles.

Table 4
Temperature related peak maxima (T_{max}) associated with TPD (to 1273 K), pre- and post-HDC with the corresponding quantity of H_2 desorbed per gram of catalyst over the 500–750 K range

	Pre-HDC		Post-HDC	
	T_{max} (K)	H_2 desorbed 500–750 K ($\mu mol\ g^{-1}$)	T_{max} (K)	H_2 desorbed 500–700 K ($\mu mol\ g^{-1}$)
Pd/SiO_2	580, **930**, **1273**	7	**1000**, 1150, 1273	–[a]
Yb/SiO_2	**1000**, **1273**	–[a]	–[b]	–[b]
$Pd–Yb/SiO_2$-step	610, **1039**, 1180	8	**973**, 1273	–[a]
$Yb–Pd/SiO_2$-step	500–750, **1021**, 1100, 1210, 1273	16	**573**, **953**, 1260	17
$Yb/Pd/SiO_2$-sim	**627**, **896**, 1273	32	**563**, **893**, 1273	40

T_{max} for principal peaks are given in bold.
[a] Below detection limit (< 1 $\mu mol\ g_{cat}^{-1}$).
[b] HDC inactive.

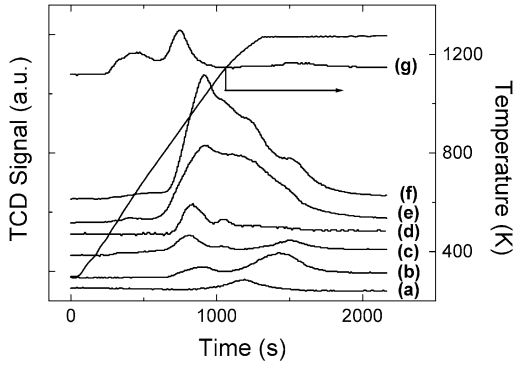

Fig. 3. H_2 TPD associated with the pre-HDC samples: (a) SiO_2, (b) Yb/SiO_2, (c) Pd/SiO_2, (d) $Pd/SiO_2 + Yb/SiO_2$, (e) $Pd–Yb/SiO_2$-step, (f) $Yb–Pd/SiO_2$-step, (g) $Yb/Pd/SiO_2$-sim.

Hydrogen temperature-programmed desorption (TPD) can shed some light on differences in metal/support interaction and electronic properties of supported metal particles [48,67]; the H_2 TPD (up to 1273 K) profiles are presented in Fig. 3, with pertinent H_2 release and T_{max} values given in Table 4. Each desorption profile is featureless at $T < 450$ K, and the absence of a H_2 release peak at 360–370 K due to Pd hydride decomposition, observed during TPR (see Fig. 1), is consistent with an exclusive H_2 chemisorption during pulse titration (i.e., no hydride formation). With the exception of Yb/SiO_2, each catalyst exhibited an ill-defined H_2 desorption peak over the temperature range of 500–750 K. Whereas this peak represented a significant proportion of the H_2 released from $Yb/Pd/SiO_2$-sim, the relative contribution for the other Pd-containing samples was considerably less. Each profile was characterized by a significant higher-temperature release of H_2 spanning the range 900–1050 K for Pd/SiO_2, Yb/SiO_2, and $Yb/Pd/SiO_2$-sim and extending into the final isothermal hold (1273 K) with shoulders to the main peak for $Pd–Yb/SiO_2$-step and $Yb–Pd/SiO_2$-step. Both Pd/SiO_2 and Yb/SiO_2 showed appreciable H_2 release at 1273 K, with distinct peaks arising in the final isothermal hold. A direct comparison of the H_2 TPD profiles generated in this study with the limited reports in the literature relating to supported Pd systems is problematic given the differences in metal loading/support/preparation/activation/desorption procedures. Sandoval and Gigola [91] recorded three peaks in their H_2 TPD (at 415, 489, and 550 K) from Pd/SiO_2 and attributed these to interaction with different Pd sites. Sepúlveda and Fígoli [90] observed a removal of weakly held H_2 from Pd/SiO_2 at 273–500 K. The appearance of multiple TPD peaks has also been attributed to desorption of "readsorbed hydrogen" [90,102], whereas peaks at $T_{max} \approx 973$ K have been ascribed to spillover hydrogen [103]. Imamura et al. [78] recorded a TPD profile for unreduced Yb/MnO (prepared by impregnation from liquid NH_3) with a peak at ca. 400 K due to H_2 release accompanied by NH_3 and N_2 as a result of the decomposition of $Yb(NH_2)_3/Yb(NH_2)_2$, with a second H_2 release at ca. 620 K due to the decomposition of the intermediate YbNH (imide). The same group [104] reported a quite different TPD response associated with Yb/activated carbon reduced at 423 K, characterized by a broad peak (at 373–1073 K) that incorporated H_2 release (leading to nonstoichiometric YbH_x) along with NH_3 and N_2. Such observations serve to demonstrate the manner by which Yb loading/pretreatment and the nature of the support can influence TPD behavior. In this study, TPD of Yb/SiO_2 generated two peaks, with $T_{max} = 1000$ and 1273 K, that can be tentatively ascribed to combined $Yb(NH_2)_x/YbH_2$ decomposition [78,104,105] and the possible desorption of spillover hydrogen. A contribution due to dehydroxylation of SiO_2 at elevated temperatures [106,107] should also be considered; the TPD of the H_2 heat-treated SiO_2 support (Fig. 3a) exhibited a significant TCD response. A proposed scheme that can account for the observed TPD profile is shown in Fig. 4. The TPD generated for $Pd/SiO_2 + Yb/SiO_2$ exhibited characteristics of both

$$YbH_2 \xrightarrow{\text{TPD to 1000 K}} YbH_x + Yb + H_2$$

$$Yb/SiO_2 \xrightarrow{\text{TPR to 573 K}} + \xrightarrow{\text{TPD to 1273 K}} \text{spillover H}$$

$$Yb(NH_2)_x \xrightarrow{\text{TPD to 1000 K}} YbNH + N_2 + H_2 \xrightarrow{\text{TPD to 1273 K}} YbN + H_2$$

Fig. 4. Schematic representation of the steps involved in TPD (ultimately to 1273 K) of Yb/SiO_2. Presence of $Yb(NH_2)_x$ and YbH_2 in the sample post TPR (to 573 K) is established by XRD; see Fig. 2.

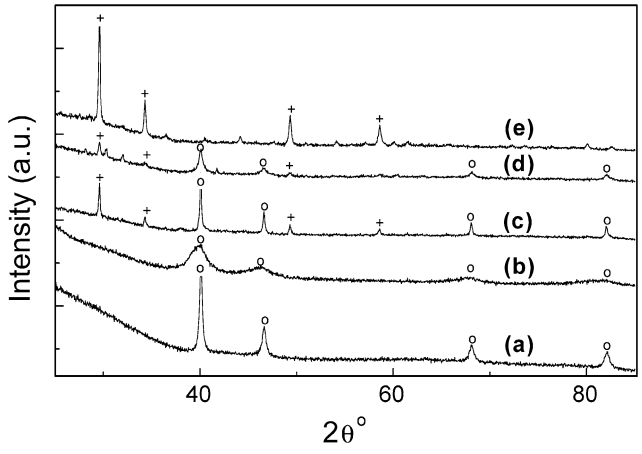

Fig. 5. XRD of the catalysts reduced at 873 K, pre-HDC: (a) Pd/SiO_2, (b) $Yb/Pd/SiO_2$-sim, (c) $Pd–Yb/SiO_2$-step, (d) $Yb–Pd/SiO_2$-step, (e) Yb/SiO_2. O indicates peak assignment for Pd (*fcc*) and + for YbH_2 (*fcc*).

components in the mixture. The H_2 released (Table 4) by the Pd and Pd/Yb systems over the range of 500–750 K matches that taken up in the chemisorption step preceding TPD (Table 3). The higher uptake and associated H_2 release over a T range comparable to the HDC reaction conditions which characterizes $Yb/Pd/SiO_2$-sim and $Yb–Pd/SiO_2$-step will be shown to have significant implications for catalytic activity. The broad (850–1273 K) and intense H_2 TPD peaks that characterize $Pd–Yb/SiO_2$-step and $Yb–Pd/SiO_2$-step must be the result of surface interaction between the Pd and Yb component and represent composite H_2 release, along the lines suggested by Imamura et al. [104], where the presence of surface Pd can impact on $Yb(NH_2)_x$ decomposition and H_2 release from surface hydride. The H_2 TPD profile generated for $Pd–Yb/SiO_2$-step and $Yb–Pd/SiO_2$-step are essentially equivalent where $T > 800$ K, suggesting that H_2 release characteristics are insensitive to the sequence of metal addition, but the nature of the precursor is critical. XRD analysis of the catalysts after thermal treatment (in H_2) at 873 K was performed to probe the bulk structure resulting from thermal treatment; the resultant patterns are shown in Fig. 5. Pd/SiO_2 exhibits sharper diffraction peaks relative to reduction at 573 K (see Fig. 2), consistent with thermally induced metal sintering. The absence of any signal due to $Yb(NH_2)_x$ is in accordance with a decomposition during TPD with any Yb_2O_3 (present after reduction at 573 K) or YbH_2-*orthorhombic* converted to *fcc* YbH_2, which was also noted by Imamura et al. [104]. $Yb/Pd/SiO_2$-sim, prepared from the organometallic precursor, exhibited a TPD response comparable to Pd/SiO_2 but with a greater quantity of surface hydrogen, which is suggestive of some surface synergism between Yb/Pd involving hydride formation/H_2 transfer; the XRD pattern was largely unaffected by the higher-temperature treatment.

3.1.3. TEM/XPS

TEM analysis of Pd/SiO_2 confirmed that the supported Pd was present as pseudospherical particles. We have previously presented representative TEM images of $Yb/Pd/SiO_2$-sim [71] that demonstrated a near-spherical Pd particle morphology, where EDX mapping revealed the presence of Yb in every

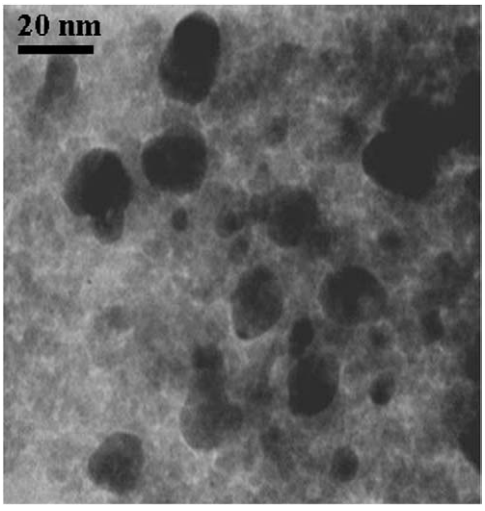

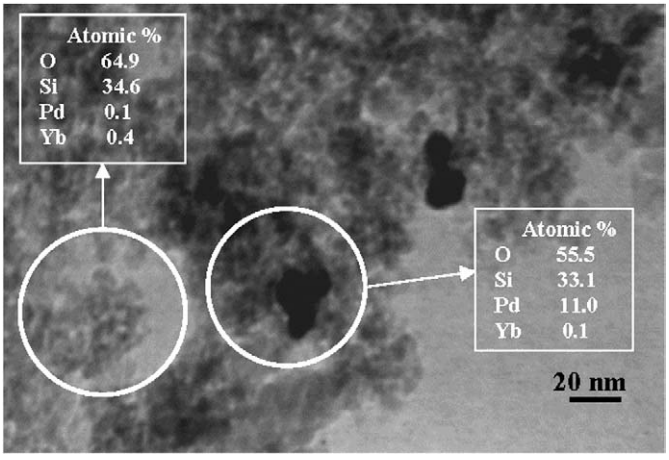

Fig. 6. Representative TEM images of $Pd–Yb/SiO_2$-step pre-HDC with the atomic compositions resulting from EDX mapping over two identified areas.

area subjected to EDX analysis even where there was no detectable Pd, findings that led us to assert that Yb is present in $Yb/Pd/SiO_2$-sim as a "thin film." Numerous TEM–EDX analyses of Yb/SiO_2 yielded surface Yb compositions that spanned the range 0.4–0.9 atom%, but we could not isolate any discrete Yb particles or clusters. The Yb component was present as a well-dispersed phase, consistent with the low BET area demonstrated in Table 1. The representative TEM images of $Pd–Yb/SiO_2$-step shown in Fig. 6 clearly demonstrate the presence of Pd particles with some morphological diversity, and the EDX analysis reveals low Yb surface content associated with the Pd particles and also in the area removed from the particles, a response characteristic of all of our TEM–EDX measurements. The $Yb–Pd/SiO_2$-step sample displayed similar behavior (i.e., pseudospherical Pd formations with no evidence of Yb particles), but in this case we found a number of areas in which the Yb content was below the limit of detection. The TEM-derived (number) weighted mean Pd particle size and range of Pd sizes detected are given in Table 5, as are values obtained from XRD analysis using the standard Scherrer line-broadening approach. The Pd sizes generated using both techniques are in reasonable agreement, and the Pd component in the bimetallic samples is

Table 5
Average Pd particle sizes from TEM and XRD analyses with range of particle sizes determined by TEM

	TEM (nm) Number averaged (range)	XRD (nm)
Pd/SiO_2	36 (<2 to 50)	33
$Pd–Yb/SiO_2$-step	15 (<5 to 30)	11
$Yb–Pd/SiO_2$-step	9 (<2 to 35)	13
$Yb/Pd/SiO_2$-sim	6 (<2 to 15)	–[a]

[a] XRD peaks too broad for accurate Pd size measurement.

present as smaller particles. The latter observation finds support in the work of Seoane et al. [89], in which the addition of lanthanum resulted in smaller Pd particles supported on SiO_2. The incorporation of Yb appeared to limit Pd sintering, possibly contributing (in part) to the enhanced H_2 chemisorption on $Yb/Pd/SiO_2$-sim and $Yb–Pd/SiO_2$-step (Table 3).

XPS spectra of the reduced/passivated samples over the Pd and Yb binding energy regions are shown in Figs. 7 and 8, respectively. The binding energies associated with the Pd $3d_{5/2}$ and Yb $4d_{5/2}$ signals, along with the atomic ratios for the bimetallic samples, are given in Table 6a. The XPS spectrum for Pd/SiO_2 is characterized by two peaks (at 330–345 eV), where the associated Pd $3d_{5/2}$ binding energy is in good agreement with values quoted in the literature [85,89]. Given the equivalency of the Pd $3d_{5/2}$ binding energies, there was no measurable electron transfer in $Yb/Pd/SiO_2$-sim relative to Pd/SiO_2. A decrease in the binding energies by 0.3 eV for both the stepwise catalysts compared with Pd/SiO_2 suggests some electron donation from the electropositive Yb. This binding energy shift is comparable to that (0.1–0.7 eV) recorded by Seoane et al. [89] for coimpregnated $La–Pd/SiO_2$. At this Yb loading, the XPS response is characterized by a rather ill-defined Yb $4d_{5/2}$ signal; representative spectra are included in Fig. 8. It was not possible to obtain a meaningful Yb/Pd atomic ratio for the bimetallic catalysts prepared by the stepwise route due to low signal intensity. The binding energy, where measurable, is close to that reported for Yb^{3+} (185 eV for Yb_2O_3) [108]. The Yb signal associated with $Yb/Pd/SiO_2$-sim, albeit weak, delivered a Yb/Pd surface atomic ratio close to the bulk ratio. Surface Yb/Pd atomic ratios resulting from EDX analysis of larger areas (ca. 4×10^5 nm^2) are also given in Table 6a; the stepwise samples exhibited a dominant surface Pd content, whereas $Yb/Pd/SiO_2$-sim displayed significant surface Yb.

3.2. HDC activity/selectivity

The HDC of CB over each catalyst generated benzene, whereas the conversion of DCB produced CB as a partially

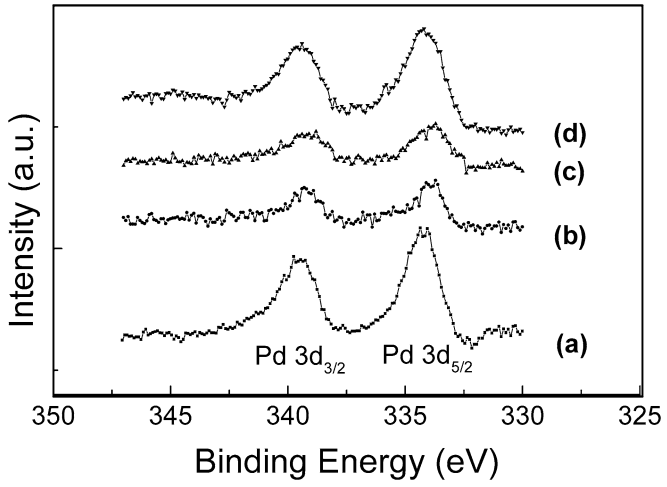

Fig. 7. Pd 3d doublet region of the XPS spectra associated with the catalysts pre-HDC: (a) Pd/SiO_2, (b) $Pd–Yb/SiO_2$-step, (c) $Yb–Pd/SiO_2$-step, (d) $Yb/Pd/SiO_2$-sim.

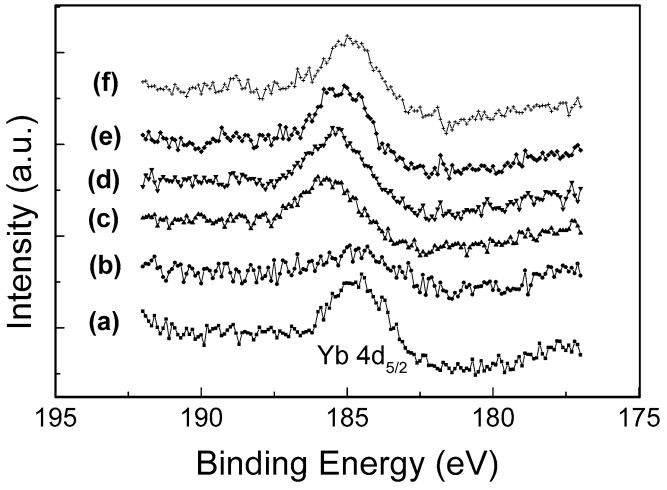

Fig. 8. XPS spectra over the Yb $4d_{5/2}$ region for: (a) Yb/SiO_2, pre-HDC; (b) $Yb/Pd/SiO_2$-sim, pre-HDC; (c) $Pd–Yb/SiO_2$-step, post-HDC; (d) $Yb–Pd/SiO_2$-step, post-HDC; (e) $Yb/Pd/SiO_2$-sim, post-HDC; (f) $YbCl_3 + SiO_2$.

Table 6a
Pd, Yb, and Cl binding energies (eV) and atomic ratios from XPS analysis of the pre- and post-HDC catalysts; surface Yb/Pd ratios from TEM–EDX analysis also included

	Pre-HDC			Post-HDC						
	Binding energy (eV)		Atomic ratio	Binding energy (eV)			Atomic ratio			
	Pd $3d_{5/2}$	Yb $4d_{5/2}$	Yb/Pd	Pd $3d_{5/2}$		Yb $4d_{5/2}$	Cl $2p_{3/2}$	Yb/Pd	Cl/Pd	Cl/(Yb + Pd)
Pd/SiO_2	334.3	–	–	334.3		–	–	–	–	–
$Pd–Yb/SiO_2$-step	334.0	–[a]	–[a] (0.1)[b]	334.2	336.7	185.8	197.8	1.3	3.2	1.4
$Yb–Pd/SiO_2$-step	334.0	–[a]	–[a] (<0.1)[b]	334.0	336.6	185.4	197.7	1.6	7.4	2.9
$Yb/Pd/SiO_2$-sim	334.3	184.8	0.6 (0.9)[b]	334.4	336.7	185.2	197.7	0.8	4.2	2.3

[a] Yb XPS signal below detection limit.
[b] From TEM–EDX analysis.

Table 6b
Pd, Yb, and Cl binding energies (eV) and atomic ratios for model samples

	Binding energy (eV)			Atomic ratio		
	Pd $3d_{5/2}$	Yb $4d_{5/2}$	Cl $2p_{3/2}$	Yb/Pd	Cl/Pd	Cl/Yb
$PdCl_2 + SiO_2$	334.4, 336.2	–	196.9	–	1.6	–
$YbCl_3 + SiO_2$	–	185.2	197.3	–	–	3.3

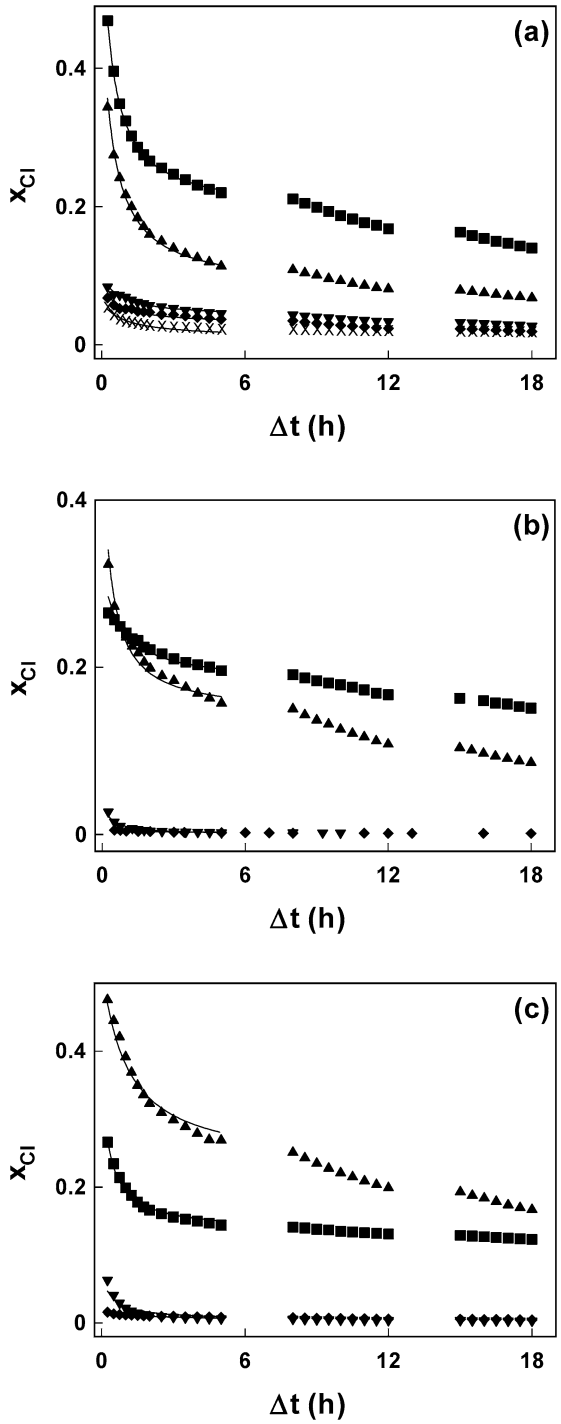

Fig. 9. Fractional dechlorination (x_{Cl}) of (a) CB, (b) 1,2-DCB, and (c) 1,3-DCB as a function of time-on-stream over Pd/SiO_2 (◆), $Pd/SiO_2 + Yb/SiO_2$ (×), Pd–Yb/SiO_2-step (▼), Yb–Pd/SiO_2-step (▲), and $Yb/Pd/SiO_2$-sim (■). Inlet hourly Cl/Pd mole ratio $= 5 \times 10^3$; $T = 423$ K. Lines represent fits to Eq. (4), correlation coefficients >0.992.

Table 7
Initial fractional dechlorination (x_0, dimensionless) and initial specific dechlorination rate (r_0, $mol_{Cl}\,h^{-1}\,m^{-2}$) of CB, 1,2-DCB, and 1,3-DCB, fractional dechlorination after 18 h on-stream ($x_{18\,h}$), the time required for the fractional dechlorination to drop to 60% of the initial value ($\Delta t_{0.6}$), and the initial selectivity to CB (S_{CB}) in the conversion of both DCB isomers: inlet hourly Cl/Pd mole ratio $= 5 \times 10^3$; $T = 423$ K

	Pd/SiO_2	Pd–Yb/SiO_2-step	Yb–Pd/SiO_2-step	Yb/Pd/SiO_2-sim
CB feed				
x_0 (r_0)	0.08 (0.24)	0.13 (0.21)	0.52 (0.46)	0.64 (0.41)
$x_{18\,h}$	0.02	0.03	0.07	0.14
$\Delta t_{0.6}$ (min)	48	41	32	52
1,2-DCB feed				
x_0 (r_0)	0.01 (0.02)	0.04 (0.05)	0.49 (0.44)	0.35 (0.23)
$x_{18\,h}$	<0.01	<0.01	0.09	0.15
$\Delta t_{0.6}$ (min)	78	55	70	145
S_{CB} (%)	81	76	20	20
1,3-DCB feed				
x_0 (r_0)	0.02 (0.06)	0.07 (0.10)	0.54 (0.49)	0.34 (0.22)
$x_{18\,h}$	<0.01	<0.01	0.17	0.12
$\Delta t_{0.6}$ (min)	95	48	93	109
S_{CB} (%)	100	50	24	29

dechlorinated product in addition to benzene. Cyclohexane was detected in only trace quantities (<0.1% conversion), a selectivity response that finds agreement in other published studies [30,53,58]. Fig. 9 illustrates fractional HDC (x_{Cl}) as a function of time on stream; reaction over Yb/SiO_2 resulted in a negligible conversion (i.e., $x_{Cl} < 0.01$). In all cases, there was a temporal drop in the level of HDC, which can be expressed in terms of the empirical relationship

$$\frac{(x_{Cl} - x_0)}{(x_{5\,h} - x_0)} = \frac{\Delta t}{(\beta + \Delta t)}. \tag{4}$$

Fit convergence (over the first 5 h on stream) yielded values for x_0, the initial fractional HDC, where $x_{5\,h}$ represents the fractional conversion after 5 h and β is a time scale fitting parameter. The associated time ($\Delta t_{0.6}$) required for the fractional dechlorination to decay to 60% of its initial value is recorded in Table 7, along with x_0 and fractional HDC after 18 h on stream ($x_{18\,h}$), as useful indices on which to base a comparison of catalyst activity and stability. Temporal CB HDC plots coincided for reactions over Pd/SiO_2, $Pd/SiO_2 + Yb/SiO_2$, and Pd–Yb/SiO_2-step, whereas Yb–Pd/SiO_2-step and $Yb/Pd/SiO_2$-sim delivered significantly higher x_{Cl} values. The specific initial CB HDC rate (r_0; see Table 7) increased in the order Pd–Yb/SiO_2-step ≈ Pd/SiO_2 < $Yb/Pd/SiO_2$-sim ≈ Yb–Pd/SiO_2-step. With the exception of Yb–Pd/SiO_2-step, which generated comparable x_0 (and r_0) in the conversion of the three chloroarenes, the catalysts exhibited lower activity in the conversion of both DCB

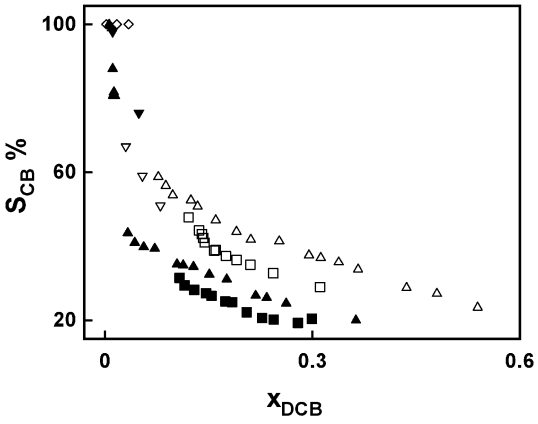

Fig. 10. CB selectivity (S_{CB} %) as a function of fractional 1,2-DCB (solid symbols) and 1,3-DCB (open symbols) conversion (x_{DCB}) for HDC over Pd/SiO_2 (◆,◇), Pd–Yb/SiO_2-step (▼,▽), Yb–Pd/SiO_2-step (▲,△), and Yb/Pd/SiO_2-sim (■,□). Inlet hourly Cl/Pd mole ratio = 5×10^3; $T = 423$ K.

isomers compared with CB. Some evidence in the literature [26,46] supports a surface HDC mechanism involving dissociative adsorption of the chloroarene with the formation of a surface σ-complex through the aromatic ring carbon with the highest electron density. The presence of a second electron-withdrawing Cl substituent in DCB serves to reduce the electron density associated with the ring carbons and lower reactivity [109]. The higher x_{Cl} recorded for 1,3-DCB relative to 1,2-DCB suggests a Cl positioning/steric contribution in which the *ortho*-positioned Cl is more resistant to scissioning from the ring than the less sterically hindered *meta*-substituted Cl, a trend that was reported previously [4]. As a general observation, loss of initial activity (at the same inlet Cl/Pd ratio) was less appreciable (see the higher $\Delta t_{0.6}$ values in Table 7) during processing of the disubstituted chloroarenes. A difference in reaction pathway emerges from the plot of CB selectivity (S_{CB}) as a function of fractional conversion of DCB (x_{DCB}), shown in Fig. 10, where the lower S_{CB} at a given x_{DCB} that characterizes 1,2-DCB HDC indicates a greater contribution due to concerted removal of both Cl substituents from the ring as opposed to stepwise HDC. The difference in catalyst performance is also evident from Fig. 10, where conversion over Pd/SiO_2 and Pd–Yb/SiO_2-step is so much lower than that delivered by Yb–Pd/SiO_2-step and Yb/Pd/SiO_2-sim that there is no overlap between the datasets. We have made an extensive search of the available literature on catalytic CB and DCB HDC and, where feasible, compiled the available rate data, which are summarized in Table 8, in which the metal loading, reaction phase, and temperature are identified and rates are expressed in the units provided in the pertinent publication. Taking Yb–Pd/SiO_2-step as a representative catalyst from this work, initial HDC rates were recorded using two sets of units that provide a meaningful link with literature values. It can be seen that our bimetallic system compares favorably with the archival gas-phase catalytic HDC rates.

It is immediately apparent that Yb acted as a HDC promoter through a surface synergism with Pd, where the extent of this promotion depends on the nature of the catalyst precursor and sequence of metal(s) introduction to the support. The specific HDC rates were significantly enhanced (by up to a factor of 25) with a concurrent or subsequent addition of Yb (Yb/Pd/SiO_2-sim and Yb–Pd/SiO_2-step), whereas Pd/SiO_2 and Pd–Yb/SiO_2-step exhibited equivalent HDC activities; that is, Pd impregnation of SiO_2 or Yb/SiO_2 was ultimately indistinguishable in terms of HDC performance. Whereas an unambiguous link between catalyst structure and HDC activity has yet to emerge from the available literature, various published studies have demonstrated a dependence of HDC activity and stability on metal dispersion in which a higher turnover frequency has been proposed for larger Pd particles, a response attributed to an ensemble effect [61]. Given that Pd/SiO_2, which has the larger Pd particles (see Table 5), delivered lower specific HDC rates, such an ensemble effect does not appear to apply in this case. Rather, the involvement of a surface Yb/Pd synergism resulting from the action of YbH_2, which serves as an additional source of surface reactive hydrogen, seems to be operative. The presence of YbH_2 was confirmed by XRD (Figs. 2 and 5), and the viability of H_2 transfer can be assessed from the TPD for both Yb–Pd/SiO_2-step and Yb/Pd/SiO_2-sim (Fig. 3). The two most active catalysts (Yb–Pd/SiO_2-step and Yb/Pd/SiO_2-sim) exhibited the greatest H_2 uptake, reflected by the amount of H_2 release at 500–750 K (Table 4); the promotional effect may be ascribed to effective surface H_2 uptake/transfer. The higher x_0 (and r_0) values delivered by Yb/Pd/SiO_2-sim and Yb–Pd/SiO_2-step in the HDC of CB can be attributed to enhanced H_2 uptake/release characteristics. The reason for the significantly higher specific activities exhibited by Yb–Pd/SiO_2-step in DCB HDC is not immediately obvious but must be linked to differences in surface composition/structure. Yb/Pd/SiO_2-sim was characterized by a thin Yb covering in intimate contact with discrete Pd particles, whereas Yb–Pd/SiO_2-step had larger Pd particles with a lower surface Yb/Pd ratio (Table 6). The observed slight shift in Pd $3d_{5/2}$ binding energy exhibited by Yb–Pd/SiO_2-step, which was not evident for Yb/Pd/SiO_2-sim, may be significant in terms of HDC promotion via electronic effects. At this juncture, we can only flag this apparent structure sensitivity where the HDC response is dependent on both the reactant (CB vs. DCB) and metal precursor.

As an addendum to the HDC studies, we examined the hydrogenation of benzene (to cyclohexane) over the same catalysts to establish a possibly generic enhanced "hydroprocessing" capability for the Yb–Pd system. In common with the HDC system, cyclohexane yield from the freshly activated Yb–Pd/SiO_2-step and Yb/Pd/SiO_2-sim was significantly higher, as recorded in Table 9, and the sequence of increasing activity again matched that of H_2 uptake. This observation is in line with the work of Imamura et al. [75], who reported enhanced C_3H_4 hydrogenation due to increased hydrogen uptake through the incorporation of Yb in Pd/SiO_2.

3.3. Catalyst characterization post-HDC

Because each catalyst exhibited a time-on-stream HDC activity loss, the used catalysts were also subjected to characterization to account for this decline in performance. Whereas the BET surface areas of each used catalyst were lower than the corresponding values for the unused samples, the differences were

Table 8
A compilation of catalytic CB, 1,2-DCB, and 1,3-DCB HDC rates as reported in the literature

Catalyst	Metal loading (reaction phase)	Reactant	T (K)	Rate	Ref.
Pd/γ-Al_2O_3	1% w/w (liquid)	CB	294	0.5×10^{-5} mol_{CB} min^{-1} g_{cat}^{-1}	[15]
		1,2-DCB		0.6×10^{-5} mol_{DCB} min^{-1} g_{cat}^{-1}	
Pd/C	5% w/w (liquid)	1,2-DCB	323	4.6 mol_{DCB} s^{-1} mol_{Pd}^{-1}	[24]
		1,3-DCB		4.8 mol_{DCB} s^{-1} mol_{Pd}^{-1}	
Raney Ni	50% w/w (liquid)	1,2-DCB	323	2.2×10^{-3} mol_{DCB} s^{-1} mol_{Ni}^{-1}	[24]
		1,3-DCB		1.8×10^{-3} mol_{DCB} s^{-1} mol_{Ni}^{-1}	
Pd/C	5% w/w (liquid)	CB	573	0.2×10^{-3} mol_{CB} l^{-1} min^{-1} g_{cat}^{-1}	[25]
Pd/Al_2O_3	0.5% w/w (gas)	CB	523	78 $mmol_{CB}$ min^{-1} g_{cat}^{-1}	[28]
		1,2-DCB		92 $mmol_{DCB}$ min^{-1} g_{cat}^{-1}	
Pd/$TiZrAlO_x$	2% w/w (gas)	1,2-DCB	523	0.05 mol_{DCB} g_{cat}^{-1} min^{-1}	[30]
Ni/SiO_2	6.1% w/w (gas)	CB	573	11×10^{-3} mol_{Cl} h^{-1} g_{cat}^{-1}	[42]
		1,2-DCB		6×10^{-3} mol_{Cl} h^{-1} g_{cat}^{-1}	
		1,3-DCB		8×10^{-3} mol_{Cl} h^{-1} g_{cat}^{-1}	
Pd/Al_2O_3	0.8% w/w (gas)	CB	353	8×10^{-6} mol_{CB} s^{-1} g_{cat}^{-1}	[50]
Rh/Al_2O_3	1% w/w (gas)	CB	353	10×10^{-8} mol_{CB} s^{-1} g_{cat}^{-1}	[50]
Ni–Mo/γ-Al_2O_3	3% w/w NiO (gas)	CB	573	1.8×10^{-4} mol_{CB} min^{-1} g_{cat}^{-1}	[52]
	23% w/w MoO_3	1,2-DCB		1.8×10^{-4} mol_{DCB} min^{-1} g_{cat}^{-1}	
Pd/GNF	8% w/w (gas)	CB	423	0.11 mol_{Cl} h^{-1} m^{-2}	[55]
Pd/AC				0.09 mol_{Cl} h^{-1} m^{-2}	
Pd/graphite				0.05 mol_{Cl} h^{-1} m^{-2}	
Pd–Fe/MgO	5% w/w Pd	CB	413	12×10^{-6} mol_{CB} s^{-1} g_{cat}^{-1}	[59]
	5% w/w Fe (gas)				
Ni/γ-Al_2O_3	10% w/w (gas)	CB	523	1.9×10^{-6} mol_{CB} s^{-1} g_{cat}^{-1}	[62]
		1,2-DCB		0.3×10^{-6} mol_{DCB} s^{-1} g_{cat}^{-1}	
		1,3-DCB		0.3×10^{-6} mol_{DCB} s^{-1} g_{cat}^{-1}	
Yb–Pd/SiO_2-step	5% w/w (gas)	CB	423	0.46 mol_{Cl} h^{-1} m^{-2}	This work
				0.020 mol_{Cl} min^{-1} g_{cat}^{-1}	
		1,2-DCB		0.44 mol_{Cl} h^{-1} m^{-2}	
				0.019 mol_{Cl} min^{-1} g_{cat}^{-1}	
		1,3-DCB		0.49 mol_{Cl} h^{-1} m^{-2}	
				0.021 mol_{Cl} min^{-1} g_{cat}^{-1}	

not significant (see Table 1). The representative TEM images of the stepwise-prepared bimetallics shown in Fig. 11 clearly reveal surface structural changes, with Pd sintering and the accretion of Pd particles evident. The conglomeration or clustering of Pd particles in Yb–Pd/SiO_2-step (Fig. 11a) and Pd–Yb/SiO_2-step (Fig. 11b) post-HDC was not observed to the same extent in the samples pre-HDC. A wider distribution of Pd particles sizes was one definite result of HDC, with Pd particles up to 60 nm isolated in the spent bimetallic catalysts. The sequence of increasing average Pd sizes – Yb/Pd/SiO_2-sim (10 nm) < Yb–Pd/SiO_2-step (18 nm) < Pd–Yb/SiO_2-step (25 nm) < Pd/SiO_2 (48 nm) – matches that recorded pre-HDC, but the particle sizes were consistently greater after reaction (see Table 5).

Catalyst poisoning can result from the formation of surface Pd and/or Yb chloride; it is known that HCl can decompose YbH_2 to release H_2 and generate $YbCl_3$ [110]. Indeed, the representative TEM–EDX analysis shown in Fig. 11c reveals an appreciable Cl content associated with the spent catalyst; Cl contents of up to 3.3 atom% were recorded. The presence of residual surface Cl in post-HDC samples was confirmed from XPS analysis with the emergence of a Cl $2p_{3/2}$ signal, as shown

Table 9
Cyclohexane yield from the hydrogenation of benzene over the pre- and post-HDC (after contact with 0.3 mol of 1,2-DCB) catalysts: $T = 423$ K; inlet hourly C_6H_6/Pd mole ratio = 35

	$Y_{cylohexane}$ (%)	
	Pre-HDC	Post-HDC
Pd/SiO_2	5	1
Pd–Yb/SiO_2-step	4	1
Yb–Pd/SiO_2-step	30	4
Yb/Pd/SiO_2-sim	38	36

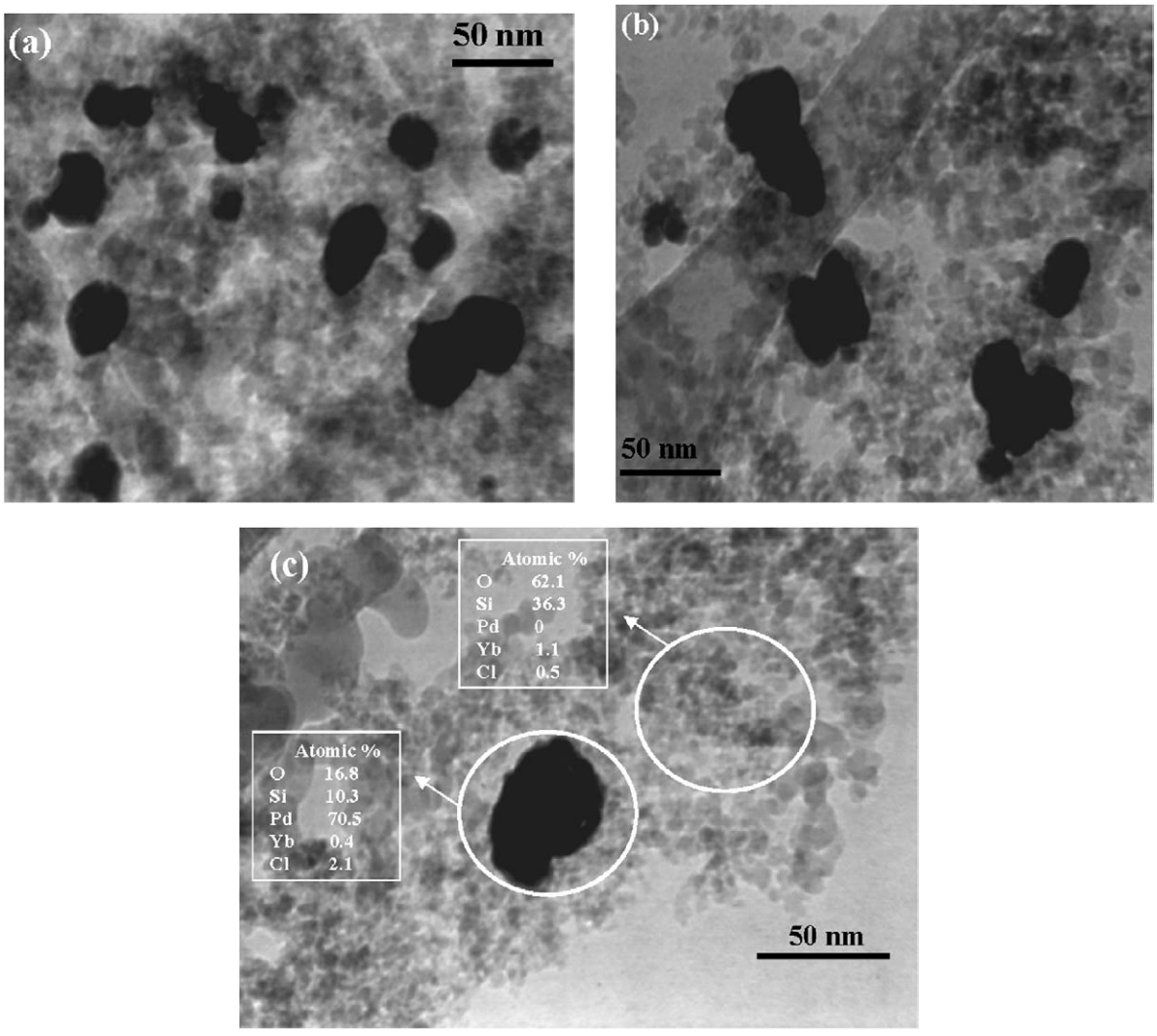

Fig. 11. Representative TEM images of the stepwise bimetallic catalysts post-HDC: (a) Yb–Pd/SiO_2-step, (b) Pd–Yb/SiO_2-step, (c) Pd–Yb/SiO_2-step with the atomic compositions resulting from EDX mapping over two identified areas.

in Fig. 12. There was no evidence of any bulk chloride formation on the basis of XRD analysis. It is noteworthy that there was no detectable XPS signal for Cl in the post-HDC Pd/SiO_2 sample. Moreover, the XPS spectrum for the used Pd/SiO_2 (Fig. 13) is indistinguishable from that recorded for the sample pre-HDC (Fig. 7), characterized by distinct Pd $3d_{3/2}$ and Pd $3d_{5/2}$ signals with identical binding energies (Table 6a). The HCl formed during HDC over Pd/SiO_2 must be swept away by the carrier gas with no measurable residual surface Cl incorporation.

Site blocking by occluded halogenated coke species is a possible cause of the observed temporal activity loss, as has been suggested elsewhere [65,111]. Indeed, it is well established [112,113] that appreciable coking accompanies hydroprocessing of Cl-containing feed, and elsewhere [49,114,115] we have demonstrated significant carbon deposition on supported Ni catalysts used in HDC applications. The Pd XPS signal for the used bimetallic catalysts exhibited a marked disruption compared with the response pre-HDC, as evident in the spectra shown in Fig. 13. A "splitting" of the Pd $3d_{3/2}$ and Pd $3d_{5/2}$ doublet is apparent for the post-HDC samples, a feature characteristic of the XPS spectrum of $PdCl_2$, which is also shown (physical mixture with SiO_2) in Fig. 13. The binding energies for both Pd $3d_{5/2}$ peaks associated with $PdCl_2 + SiO_2$ (Table 6b) match those recorded for the three bimetallic catalysts post-HDC and are consistent with Pd^{2+} [53]. The Cl $2p_{3/2}$ binding energies (197.7 ± 0.1 eV) deviate significantly from the value (200.6 eV) recorded by Fígoli et al. [76] for SiO_2-supported $PdCl_2$ and are slightly higher than those recorded for the $PdCl_2 + SiO_2$ and $YbCl_3 + SiO_2$ standards (Table 6b). It is noteworthy that postreaction analysis of each bimetallic sample delivered a significant Yb $4d_{5/2}$ signal, as shown in Fig. 8. Given that the stepwise samples did not generate any detectable Yb XPS signal pre-HDC, this observation alone is suggestive of a surface restructuring. The Yb $4d_{5/2}$ binding energies post-HDC are shifted to higher values relative to that recorded for unused Yb/Pd/SiO_2-sim (Table 6a) to approach the value (in Table 6b) determined for $YbCl_3 + SiO_2$. Surface restructuring is also apparent from the Yb/Pd atomic ratios, where Yb/Pd/SiO_2-sim exhibited some surface enrichment by

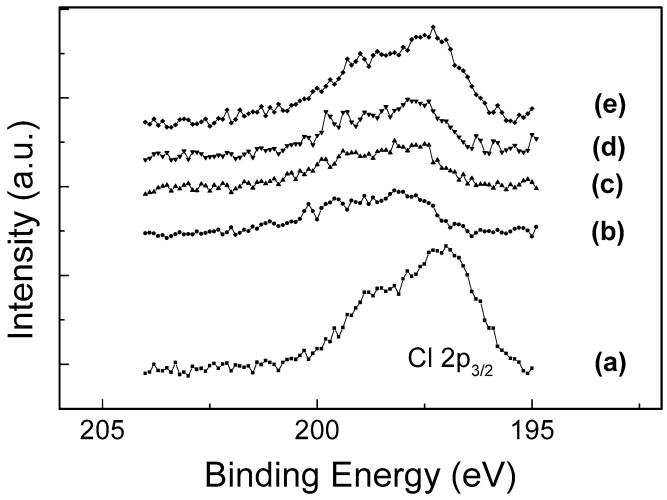

Fig. 12. XPS spectra over the Cl 2p region for: (a) $PdCl_2 + SiO_2$; (b) Pd–Yb/SiO_2-step, post-HDC; (c) Yb–Pd/SiO_2-step, post-HDC; (d) Yb/Pd/SiO_2-sim, post HDC; (e) $YbCl_3 + SiO_2$.

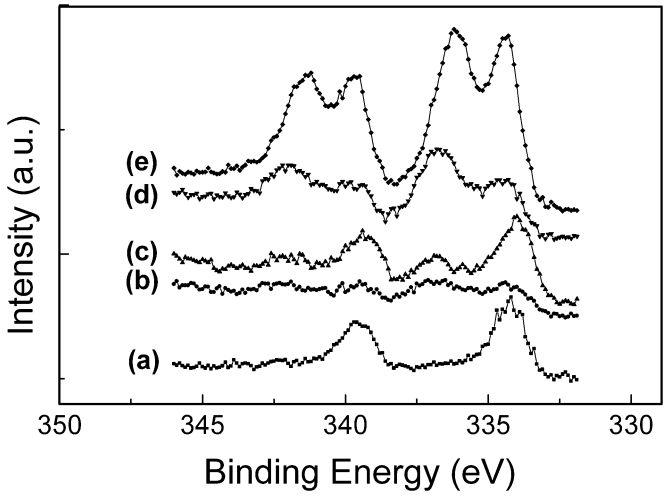

Fig. 13. Pd 3d doublet region of the XPS spectra associated with the catalysts post-HDC: (a) Pd/SiO_2, (b) Pd–Yb/SiO_2-step, (c) Yb–Pd/SiO_2-step, (d) Yb/Pd/SiO_2-sim, (e) $PdCl_2 + SiO_2$.

Yb post-HDC and both stepwise samples bore a higher proportion of Yb relative to Pd, a response in marked contrast to the unused sample. Taking the situation in which two and three Cl atoms are associated with each surface Pd and Yb, respectively, the resultant atomic ratio Cl/(Yb + Pd) equals 2.4, which is the case (and is even exceeded) by Yb–Pd/SiO_2-step and Yb/Pd/SiO_2-sim; this is diagnostic of a surface saturation by Cl during HDC. Indeed, the high Cl content associated with the used Yb–Pd/SiO_2-step and Yb/Pd/SiO_2-sim suggests a stronger surface interaction with the chlororoarene reactant and the accessible Yb component, which may play a role in activating the C–Cl bond for hydrogenolytic attack.

The TPR profiles for the spent samples were dominated by the negative peak associated with Pd hydride decomposition. The associated T_{max} and H/Pd ratios did not, in the main, deviate markedly from the values obtained for the unused bimetallics, as can be seen from the entries in Table 2. A higher H/Pd ratio was recorded for Pd/SiO_2 post-HDC relative to the unused catalyst. This can tentatively be related to Pd sintering [87,98], which is consistent with the TEM analysis and the lower H_2 uptake (Table 3); the subsequent H_2 TPD did not result in a measurable H_2 release over 500–750 K (Table 4). A lower H_2 uptake postreaction was also observed for Pd–Yb/SiO_2-step, but the used Yb–Pd/SiO_2-step and Yb/Pd/SiO_2-sim exhibited little difference in hydride decomposition response or H_2 chemisorption behavior. The H_2 consumption peaks during TPR of the passivated post-HDC bimetallic samples and subsequent H_2 TPD were shifted to lower values (Table 4), responses that must be linked to some surface restructuring/Cl inclusion resulting from HDC. Benzene hydrogenation was used as a test reaction to further probe the extent of catalyst deactivation; cyclohexane yields pre- and post-HDC are compared in Table 9. With the exception of the Yb/Pd/SiO_2-sim, each catalyst delivered appreciably lower hydrogenation activities after prolonged contact with 1,2-DCB. This decline in catalyst performance can be linked to Cl–surface interactions that impact on H_2 uptake/release dynamics. The apparent resistance exhibited by Yb/Pd/SiO_2-sim to activity loss in the benzene → cyclohexane reaction requires further investigation but is consistent with the appreciably higher $\Delta t_{0.6}$ values recorded in Table 7.

4. Conclusion

This study has shown that the presence of Yb has a significant impact on catalyst performance in the gas-phase HDC of CB, 1,2-DCB, and 1,3-DCB over SiO_2-supported Pd and Pd–Yb catalysts. CB HDC yielded benzene as the predominant product (<0.1% conversion to cyclohexane), where initial specific HDC rates increased in the order Pd/SiO_2 ≈ Pd–Yb/SiO_2-step ≪ Yb–Pd/SiO_2-step < Yb/Pd/SiO_2-sim, a sequence consistent with Yb action as a HDC promoter. This response extends to the HDC of both DCB isomers, where Yb–Pd/SiO_2-step delivered higher HDC activities than Yb/Pd/SiO_2-sim. The presence of a second electron-withdrawing Cl substituent in DCB served to lower overall reactivity relative to CB, whereas the higher fractional conversion of 1,3-DCB compared with 1,2-DCB is consistent with steric hindrance effects, where the *ortho*-positioned Cl is more resistant to HDC than the less sterically constrained *meta*-substituted Cl. Although reaction over Yb/SiO_2 resulted in negligible conversion, the combination of Yb with Pd can serve to significantly enhance the specific HDC rate (by up to a factor of 25). But the extent of this promotion depends on the nature of the catalyst precursor and sequence of metal(s) introduction to the support; a concurrent or subsequent addition of Yb (Yb/Pd/SiO_2-sim and Yb–Pd/SiO_2-step) delivered the best HDC performance. TPR of Pd/SiO_2 generated a negative (H_2 release) peak due to Pd hydride decomposition in which Yb inhibits hydride formation; the supported Pd phase thus generated exhibited an exclusive cubic symmetry. TPR of the bimetallic catalysts generated a broad higher-temperature (>530 K) region of H_2 consumption, which is attributed to Yb interactions that affect the secondary PdO reduction and/or to a possible contribution due to Yb_2O_{3+x}

reduction. The Yb–Pd/SiO_2-step and Yb/Pd/SiO_2-sim samples exhibited threefold and fivefold increases in H_2 chemisorption, respectively, relative to Pd/SiO_2 (and Pd–Yb/SiO_2-step), where the H_2 TPD response suggests a surface interaction between the Pd and Yb component to generate a composite H_2 release. XRD analysis of the activated bimetallic samples revealed the presence of YbH_2, $Yb(NH_2)_x$, and Yb_2O_3. Both TEM and XRD measurements are consistent with smaller Pd particle sizes in the bimetallic samples, whereas the XPS response suggests some electron transfer from the electropositive Yb in the stepwise-prepared samples. HDC enhancement is attributed to a greater quantity of surface hydrogen in the bimetallic samples due to a surface synergism between Yb/Pd involving hydride formation/H_2 transfer. The possibility of Yb activation of the C–Cl bond(s) for hydrogenolytic attack is also noted. This promotional effect extends to aromatic hydrogenation, as demonstrated by the higher cyclohexane yields from benzene hydrogenation over Yb–Pd/SiO_2-step and Yb/Pd/SiO_2-sim. Each catalyst was subject to a loss of HDC activity with time on stream, which can be attributed to the combined effects of HCl poisoning (residual surface Cl confirmed by TEM–EDX and XPS) and disrupted H_2 adsorption/release dynamics; we also do not discount the possible deleterious involvement of coke deposition.

Acknowledgments

This work was supported in part by National Science Foundation grants CTS-0218591 (to M.A.K.) and CHE-9901115 and CHE-0213491 (to S.G.S.).

References

[1] A.R. Pinder, Synthesis (1980) 425.
[2] V.V. Lunin, E.S. Lokteva, Russ. Chem. Bull. 45 (1996) 1519.
[3] E.-J. Shin, M.A. Keane, J. Hazard. Mater. B 66 (1999) 265.
[4] M.A. Keane, in: M.A. Keane (Ed.), Interfacial Applications in Environmental Engineering, Marcel Dekker, New York, 2002, p. 231.
[5] J.K. Fawell, S. Hunt, Environmental Toxicology, Organic Pollutants, Ellis Horwood, Chichester, 1988.
[6] Y. Liu, M. Luo, Z. Wei, Q. Xin, P. Ying, C. Li, Appl. Catal. B 29 (2001) 61.
[7] M.A. Keane, Environ. Bus. Mag. 80 (2001) 12.
[8] B. Schrick, J.L. Blough, A.D. Jones, T.E. Mallouk, Chem. Mater. 14 (2002) 5140.
[9] S. Zinovyev, A. Perosa, S. Yufit, P. Tundo, J. Catal. 211 (2002) 347.
[10] F. Murena, F. Gioia, Appl. Catal. B 38 (2002) 39.
[11] B. Aikawa, R.C. Burk, B.B. Sitholé, Appl. Catal. B 32 (2001) 269.
[12] Yu. Shindler, Yu. Matatov-Meytal, M. Sheintuch, Ind. Eng. Chem. Res. 40 (2001) 3301.
[13] P. Tundo, S. Zinovyev, A. Perosa, J. Catal. 196 (2000) 330.
[14] F. Murena, E. Schioppa, Appl. Catal. B 27 (2000) 257.
[15] C. Schüth, M. Reinhard, Appl. Catal. B 18 (1998) 215.
[16] G.V. Lowry, M. Reinhard, Environ. Sci. Technol. 33 (1999) 1905.
[17] F. Murena, J. Hazard. Mater. 75 (2000) 49.
[18] F. Murena, F. Gioia, J. Hazard. Mater. 60 (1998) 271.
[19] F. Gioia, V. Famiglietti, F. Murena, J. Hazard. Mater. 33 (1993) 63.
[20] F. Gioia, E.J. Gallagher, V. Famiglietti, J. Hazard Mater. 38 (1994) 277.
[21] G. Yuan, M.A. Keane, Chem. Eng. Sci. 58 (2003) 257.
[22] G. Yuan, M.A. Keane, Catal. Commun. 4 (2003) 195.
[23] T. Janiak, J. Błazejowski, Chemosphere 48 (2002) 1097.
[24] C.A. Marques, O. Rogozhnikova, M. Selva, P. Tundo, J. Mol. Catal. A: Chem. 96 (1995) 301.
[25] K. Konuma, N. Kameda, J. Mol. Catal. A: Chem. 178 (2002) 239.
[26] B.F. Hagh, D.T. Allen, Chem. Eng. Sci. 45 (1990) 2695.
[27] D.I. Kim, D.T. Allen, Ind. Eng. Chem. Res. 36 (1997) 3019.
[28] E. López, S. Ordóñez, H. Sastre, F.V. Díez, J. Hazard. Mater. B 97 (2003) 281.
[29] S. Ordóñez, H. Sastre, F.V. Díez, Appl. Catal. B 40 (2003) 119.
[30] A. Gampine, D.P. Eyman, J. Catal. 179 (1998) 315.
[31] S. Deshmukh, J.L. d'Itri, Catal. Today 40 (1998) 377.
[32] P.P. Kulkarni, V.I. Kovalchuk, J.L. d'Itri, Appl. Catal. B 36 (2002) 299.
[33] S. Ordóñez, F.V. Díez, H. Sastre, Ind. Eng. Chem. Res. 41 (2002) 505.
[34] B. Heinrichs, J.-P. Schoebrechts, J.-P. Pirard, J. Catal. 200 (2001) 309.
[35] R.M. Rioux, C.D. Thompson, N. Chen, F.H. Ribeiro, Catal. Today 62 (2000) 269.
[36] C.D. Thompson, R.M. Rioux, N. Chen, F.H. Ribeiro, J. Phys. Chem. B 104 (2000) 3067.
[37] E.-J. Shin, M.A. Keane, J. Chem. Technol. Biotechnol. 75 (2000) 159.
[38] E.-J. Shin, M.A. Keane, Catal. Lett. 58 (1999) 141.
[39] G. Tavoularis, M.A. Keane, J. Mol. Catal. A: Chem. 142 (1999) 187.
[40] E.-J. Shin, M.A. Keane, Chem. Eng. Sci. 54 (1999) 1109.
[41] E.-J. Shin, M.A. Keane, Appl. Catal. B 18 (1998) 241.
[42] M.A. Keane, G. Pina, G. Tavoularis, Appl. Catal. B 48 (2004) 275.
[43] G. Rupprechter, G.A. Somorjai, Catal. Lett. 48 (1997) 17.
[44] F.H. Ribeiro, C.A. Gerken, G.A. Somorjai, C.S. Kellner, G.W. Coulston, L.E. Manzer, L. Abrams, Catal. Lett. 45 (1997) 149.
[45] B.S. Ahn, S.C. Lee, D.J. Moon, B.G. Lee, J. Mol. Catal. A: Chem. 106 (1996) 83.
[46] M.A. Keane, D.Y. Murzin, Chem. Eng. Sci. 56 (2001) 3185.
[47] G. Tavoularis, M.A. Keane, J. Chem. Technol. Biotechnol. 74 (1999) 60.
[48] E.-J. Shin, A. Spiller, G. Tavoularis, M.A. Keane, Phys. Chem. Chem. Phys. 1 (1999) 3173.
[49] C. Menini, C. Park, E.-J. Shin, G. Tavoularis, M.A. Keane, Catal. Today 62 (2000) 355.
[50] B. Coq, G. Ferrat, F. Figueras, J. Catal. 101 (1986) 434.
[51] P. Bodnariuk, B. Coq, G. Ferrat, F. Figueras, J. Catal. 116 (1989) 459.
[52] B.F. Hagh, D.T. Allen, AIChE J. 36 (1990) 773.
[53] R. Gopinath, N. Lingaiah, B. Sreedhar, I. Suryanarayana, P.S.S. Prasad, A. Obuchi, Appl. Catal. B 46 (2003) 587.
[54] S.B. Halligudi, B.M. Devassay, A. Ghosh, V. Ravikumar, J. Mol. Catal. A: Chem. 184 (2002) 175.
[55] C. Amorim, G. Yuan, P.M. Patterson, M.A. Keane, J. Catal. 234 (2005) 268.
[56] R. Gopinath, K.N. Rao, P.S.S. Prasad, S.S. Madhavendra, S. Narayanan, G. Vivekanandan, J. Mol. Catal. A: Chem. 215.
[57] N. Lingaiah, P.S.S. Prasad, P.K. Rao, F.J. Berry, L.E. Smart, Catal. Commun. 3 (2002) 391.
[58] F.J. Berry, L.E. Smart, P.S.S. Prasad, N. Lingaiah, P.K. Rao, Appl. Catal. A 204 (2000) 191.
[59] N. Lingaiah, P.S.S. Prasad, P.K. Rao, L.E. Smart, F.J. Berry, Appl. Catal. A 213 (2001) 189.
[60] A.Yu. Stakheev, L.M. Kustov, Appl. Catal. A 188 (1999) 3.
[61] W. Juszczyk, A. Malinowski, Z. Karpiński, Appl. Catal. A 166 (1998) 311.
[62] A.R. Suzdorf, S.V. Morozov, N.N. Anshits, S.I. Tsiganova, A.G. Anshits, Catal. Lett. 29 (1994) 49.
[63] G. Pina, C. Louis, M.A. Keane, Phys. Chem. Chem. Phys. 5 (2003) 1924.
[64] M.A. Keane, C. Park, C. Menini, Catal. Lett. 88 (2003) 89.
[65] E.J. Creyghton, M.H.W. Burgers, J.C. Jansen, H. van Bekkum, Appl. Catal. A 128 (1995) 275.
[66] J. Estellé, J. Ruz, Y. Cesteros, R. Fernandez, P. Salagre, F. Medina, J.-E. Sueiras, J. Chem. Soc., Faraday Trans. 92 (1996) 2811.
[67] C. Park, C. Menini, J.L. Valverde, M.A. Keane, J. Catal. 211 (2002) 451.
[68] D.A. Dodson, H.F. Rase, Ind. Eng. Chem. Prod. Res. Dev. 17 (1978) 236.
[69] S. Jujjuri, E. Ding, S.G. Shore, M.A. Keane, Appl. Organomet. Chem. 17 (2003) 493.
[70] B. Coq, F. Figueras, J. Mol. Catal. A: Chem. 173 (2001) 117.
[71] S.G. Shore, E. Ding, C. Park, M.A. Keane, Catal. Commun. 3 (2002) 77.
[72] P.L. Watson, T.H. Tulip, I. Williams, Organomet. 9 (1990) 1999.

[73] Z. Xie, C. Qian, Y. Huang, J. Organomet. Chem. 412 (1991) 61.
[74] C. Qian, G. Zou, L. Gao, J. Organomet. Chem. 525 (1996) 23.
[75] H. Imamura, M. Suzuki, Y. Sakata, S. Tsuchiya, J. Alloys Compd. 303–304 (2000) 514.
[76] N.S. Fígoli, P.C. L'Argentiere, A. Arcoya, X.L. Seoane, J. Catal. 155 (1995) 95.
[77] T. Teranishi, K. Nakata, M. Iwamoto, M. Miyake, N. Toshima, React. Funct. Polym. 37 (1998) 111.
[78] H. Imamura, K. Nishimura, T. Yoshimura, H. Yoshimochi, M. Ueno, Y. Sakata, S. Tsuchiya, J. Mol. Catal. A: Chem. 165 (2001) 189.
[79] D.W. Knoeppel, J. Liu, E.A. Meyers, S.G. Shore, Inorg. Chem. 37 (1998) 4828.
[80] F.B. Noronha, M. Schmal, B. Moraweck, P. Delichère, M. Brun, F. Villain, R. Fréty, J. Phys. Chem. B 104 (2000) 5478.
[81] C.-B. Wang, H.-K. Lin, C.-M. Ho, J. Mol. Catal A: Chem. 180 (2002) 285.
[82] L.W. Konopny, A. Juan, D.E. Damiani, Appl. Catal. B 15 (1998) 115.
[83] J. Batista, A. Pintar, D. Mandrino, M. Jenko, V. Martin, Appl. Catal. A 206 (2001) 113.
[84] C. Yang, J. Ren, Y. Sun, Catal. Lett. 84 (2002) 123.
[85] P.A. Weyrich, H. Treviño, W.F. Hölderich, W.M.H. Sachtler, Appl. Catal. A 163 (1997) 31.
[86] O.E. Lebedeva, W.-A. Chiou, W.M.H. Sachtler, Catal. Lett. 66 (2000) 189.
[87] N.K. Nag, J. Phys. Chem. B 105 (2001) 5945.
[88] W. Juszczyk, Z. Karpiński, D. Łomot, J. Pielaszek, Z. Paál, A.Yu. Stakheev, J. Catal. 142 (1993) 617.
[89] X.L. Seoane, N.S. Fígoli, P.C.L. Argentiere, J.A. González, A. Arcoya, Catal. Lett. 47 (1997) 213.
[90] J.H. Sepúlveda, N.S. Fígoli, Appl. Surf. Sci. 68 (1993) 257.
[91] V.H. Sandoval, C.E. Gigola, Appl. Catal. A 148 (1996) 81.
[92] L.M. Gomez-Sainero, A. Cortes, X.L. Seoane, A. Arcoya, Ind. Eng. Chem. Res. 39 (2000) 2849.
[93] J. Murthy, S. Shekar, V. Kumar, K. Rao, Catal. Commun. 3 (2002) 145.
[94] A. Kern, W. Eysel, Mineralogisch Petrograph, Univ. Heidelberg, 1983; CAS: 7440-05-3.
[95] A.D. Ninno, V. Violante, A.L. Barbera, Phys. Rev. B 56 (1997) 2417.
[96] A. Rose, S. Maniguet, R.J. Mathew, C. Slater, J. Yao, A.E. Russell, Phys. Chem. Chem. Phys. 5 (2003) 3220.
[97] N. Nishimiya, T. Kishi, T. Mizushima, A. Matsumoto, K. Tsutsumi, J. Alloys Compd. 319 (2001) 312.
[98] F. Pinna, M. Signoretto, G. Strukul, S. Polizzi, N. Pernicone, React. Kinet. Catal. Lett. 60 (1997) 9.
[99] S. Cotton, Lanthanides and Actinides, Oxford University Press, New York, 1991, p. 17.
[100] J.C. Achard, C.N.R.S. Meudon-Bellevue, Rev. Intern. Hautes Temp. Refract. 3 (1966) 281.
[101] S.G. Shore, E. Ding, C. Park, M.A. Keane, J. Mol. Catal. A: Chem. 212 (2004) 291.
[102] J.S. Rieck, A.T. Bell, J. Catal. 85 (1984) 143.
[103] F. Benseradj, F. Sadi, M. Chater, Appl. Catal. A 228 (2002) 135.
[104] H. Imamura, Y. Maeda, T. Kumai, Y. Sakata, S. Tsuchiya, Catal. Lett. 88 (2003) 69.
[105] J.M. Haschke, M.R. Clark, High Temp. Sci. 4 (1972) 386.
[106] A.-G. Boudjahem, S. Monteverdi, M. Mercy, D. Ghanbaja, M.M. Bettahar, Catal. Lett. 84 (2002) 115.
[107] V.I. Bogillo, L.S. Pirnach, A. Dabrowski, Langmuir 13 (1997) 928.
[108] R.J. Iwanowski, M. Heinonen, I. Pracka, J. Kachniarz, Appl. Surf. Sci. 136 (1998) 95.
[109] M.A. Keane, Appl. Catal. A 271 (2004) 109.
[110] J.C. Warf, K.I. Hardcastle, Inorg. Chem. 5 (1966) 1736.
[111] L. Delannoy, J.-M. Giraudon, P. Granger, L. Leclercq, Catal. Today 59 (2000) 231.
[112] C.L. Pieck, E.L. Jablonski, R.J. Verderone, J.M. Parera, Appl. Catal. 56 (1989) 1.
[113] A. Stanislaus, B.H. Cooper, Catal. Rev. Sci. Eng. 38 (1996) 75.
[114] L.D. Cherukuri, G. Yuan, M.A. Keane, Top. Catal. 29 (2004) 117.
[115] C. Park, M.A. Keane, J. Colloid Interface Sci. 250 (2002) 37.